

Apo and Nickel-Bound Forms of the *Pyrococcus horikoshii* Species of the Metalloregulatory Protein: NikR Characterized by Molecular Dynamics Simulations[†]

Daniel J. Sindhikara, Adrian E. Roitberg, and Kenneth M. Merz, Jr.*

University of Florida, Department of Chemistry Quantum Theory Project, 2328 New Physics Building, P.O. Box 118435, Gainesville, Florida 32611-8435

Received August 2, 2009; Revised Manuscript Received November 5, 2009

ABSTRACT: NikR is a homotetrameric nickel regulatory protein whose binding to free Ni²⁺ increases its binding affinity for a gene that codes for a nickel transporter protein. It is comprised of a tetrameric nickel-binding domain, flanked by two dimeric DNA-binding domains. Though X-ray crystallography data for various species (*Escherichia coli*, *Helicobacter pylori*, and *Pyrococcus horikoshii*) of NikR reveal large conformational differences between nickel-bound, DNA-bound, and unbound forms, transitions between them have never been observed. We have run all-atom molecular dynamics simulations of three forms of the *Pyrococcus horikoshii* species of NikR including two apo-forms and one nickel-bound form. Though all 552 residues of this species occur naturally, quantum-mechanics-based force-field parametrization was required to accurately represent the four nickel-centers in the nickel-bound form. Global conformational analysis of the three 100-ns-long simulations indicates slow conformational kinetics and independent DNA binding domain motion. Correlation and flexibility analysis revealed regions of high structural and dynamical importance. A striking relationship was observed between regions with high levels of structural importance and regions with known biological importance. Mutation of key regions of *P. horikoshii* and analogous regions in both *E. coli* and *H. pylori* are suggested that might inhibit DNA-binding activity while not affecting nickel-binding.

The understanding of metal ion homeostasis at the molecular level is critical to our understanding of how toxic metal ions are delivered safely and specifically to the appropriate location within cells (1–3). There is a significant structural, biochemical, and medical literature on the homeostasis of Cu, for example, due to its role in several neurodegenerative disorders (Alzheimer's and amyotrophic lateral sclerosis (Lou Gehrig's disease), for example) (1, 2, 4–8). Despite its inherent toxicity, many microorganisms require cellular nickel as an enzyme cofactor (9, 10). *Escherichia coli* and *Helicobacter pylori*, for example, utilize nickel for [NiFe]-hydrogenases and urease, which are important for microbial energy metabolism and creation of ammonia as a nitrogen source, respectively (10, 11). NikR is a DNA-binding metalloregulatory protein that utilizes nickel-responsive allostery to modulate cellular nickel concentrations in various ways (3, 12, 13). In *E. coli*, NikR detects cellular nickel levels and selectively binds and represses the operon which encodes NikABCDE, an ABC-type membrane transporter (12, 14) effectively reducing nickel import. In *H. pylori*, NikR, activated by high nickel levels, represses expression of nickel-dependent proteins, such as the HoxN type permease (NixA) which imports nickel, while stimulating activation of other proteins (15). Hence, NikR senses intracellular levels of Ni and shuts down the production of the transporter when the level of Ni is appropriate for the cell to function (12).

[†]This work was supported by the National Institutes of Health (NIH) Grant GM066859. Simulations were performed on the Teragrid "Kraken" cluster under Grant No. MCA05S010 and the University of Florida HPC (UFHPC).

*To whom correspondence should be addressed. Tel.: 352-392-6973. Fax: 352-392-8722. E-mail: merz@qtp.ufl.edu.

ALLOSTERIC MECHANISM

It has been found that NikR's affinity for DNA is dependent on nickel concentration (16, 17). NikR contains both low (30 nM) and high-affinity (20 pM) nickel-binding sites; when the high (low) affinity nickel sites become occupied, DNA affinity increases to nanomolar (picomolar) levels (17). Carrington et al. found that nickel binds to the high affinity sites in a unique square-planar geometry, but changes to 6-coordinate when bound to DNA (18). Several species of NikR have been crystallized in various forms by Drennan and co-workers (*E. coli* NikR – EcNikR) (19, 20) Terradot and co-workers (*H. pylori* NikR – HpNikR) (21) and Chivers and Tahirov (*Pyrococcus horikoshii* NikR – PhNikR) (22). The overall structure consistently shows NikR to have a central tetrameric metal-binding domain (MBD) constructed of a $\beta\alpha\beta\alpha\beta$ ferredoxin-like fold binding nickel in square-planar geometry flanked by two dimeric ribbon-helix-helix ($\beta\alpha\alpha$) DNA binding domains (DBDs) (see Figure 1).

There are, however, some unique characteristics between different species' crystal structures. The relatively stable MBD of NikR and two rotatable DBDs of NikR can adapt roughly three different main conformations (straight, trans or cis) whose stability seems to be related to both nickel and DNA binding. We will refer to the different forms by the presence of nickel, A (apo) for nickel-free, H (holo) for nickel-bound, and the global conformation, T for trans-like, C for cis-like, and S for straight. Figure 2 shows sketches of various forms of NikR. Schreiter et al. crystallized EcNikR in AS, HS, and HC (DNA-bound) forms (19, 20, 23). They found that only the nickel-bound forms had a well-ordered α_3 helix (a helix containing one of the four

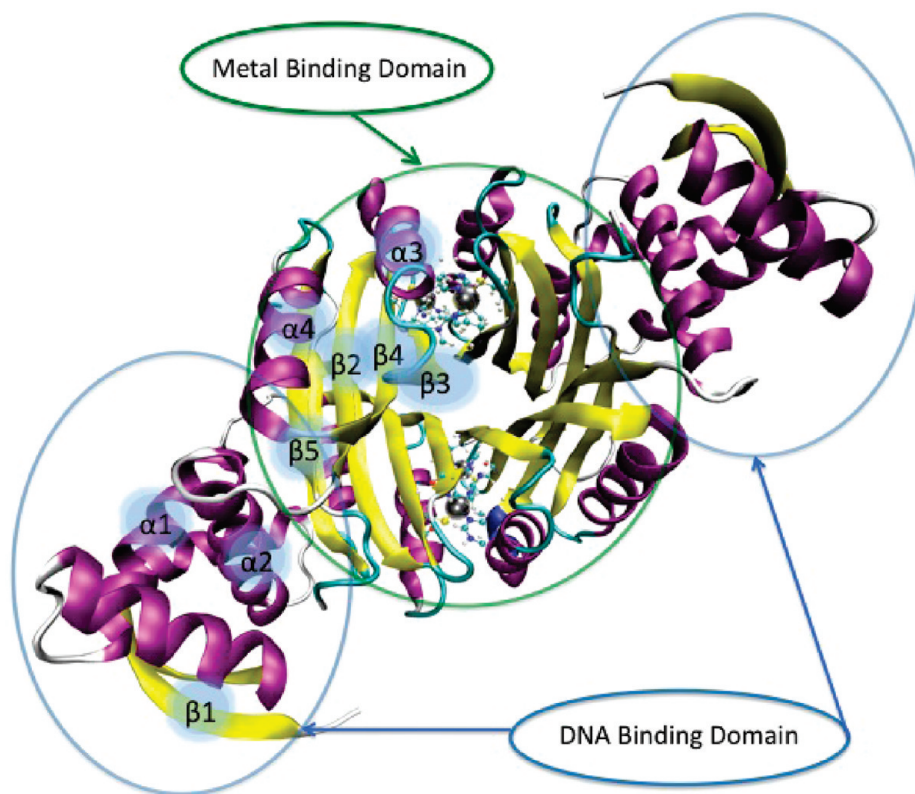


FIGURE 1: A rendering of PhNikR. The DNA binding domains ($\beta\alpha\alpha$) surround the central metal binding domain ($\beta\alpha\beta\alpha\beta$). Metallic spheres represent bound nicks.

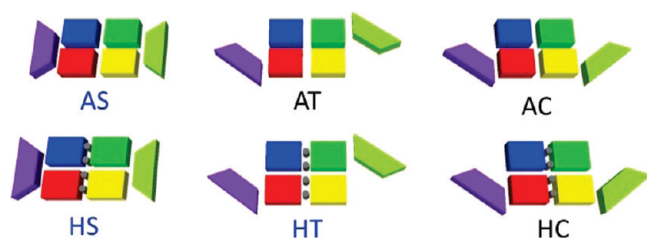


FIGURE 2: Sketch of various possible forms of NikR. Rectangles represent metal binding domains (each color represents a different chain, purple and lime represent intertwined chains). Trapezoids represent the DNA binding domains (each has contributions from two chains). Gray circles represent primary nickel binding sites. Only the three with names written in blue were found experimentally in the absence of DNA. In the cis form, NikRs DBDs snugly fit into the major groove of DNA.

nickel-binding residues). This led to the proposition that the stabilization of the $\alpha 3$ helix assists in DNA binding, a hypothesis supported by comparative metal binding studies (24). Chivers and Tahirov crystallized five forms of *P. horikoshii* including AS, HS, and three forms of HT: one with the four high affinity nickel-binding sites occupied and PhNikRs unique additional four auxiliary high affinity sites bound, one with all high and low sites bound, and one with all sites bound in the presence of free phosphate ions (to simulate DNA) (22). The AS form, similar to EcNikR, was found to have a highly mobile and disordered $\alpha 3$ -helix. Interestingly, the form with phosphate ions is oriented in a trans-form that should not fit into the corresponding DNA operon assuming that the DNA binding is similar to that of EcNikR which binds in a cis-form. As Chivers and Tahirov noted, this form can be converted into a cis-form if one-half (any two chains that share a DBD) is rotated by 180 degrees about the

center axis (turning it from a trans to a cis) (22). The crystal forms found by Dian et al. of HpNikR were the most unique set of the three species crystallized (21). They found a unique AT structure, which roughly resembles the HT form of PhNikR but lacks dimeric symmetry. Also, HpNikR was never found with all four high-affinity nickel-binding sites occupied, but rather with a single high-affinity nickel site bound per dimer, an intermediate site, or an external site. It is possible that this peculiarity could have been caused by the low pH conditions of the crystallization (21), as noted by Zambelli et al.(25)

These various permutations of conformations and nickel and DNA bound states both provide insight and raise questions about NikR's allosteric mechanism. What role does nickel binding have in the structural preference of NikR? Does nickel-binding preferentially stabilize one conformation over another otherwise in preexisting equilibrium (26)? What residues are important in promoting these conformational changes?

To elucidate the role of nickel binding on conformational states and dynamics of NikR we simulated various forms using all-atom molecular dynamics (MD) simulations. MD simulations of biological molecules have often been utilized to elucidate biological mechanisms (27). Few computational studies of any species of NikR have been reported. Cui and Merz utilized a coarse-grained Gaussian-network-model to find natural global fluctuations in PhNikR (28). They found that natural fluctuations lead to transitions between the major conformational states found in NikR crystal structures (between straight, trans, and cis). This coarse-grained study supports the pre-existing equilibrium hypothesis — that all the available conformational states are available to each bound state (26). Bradley et al. utilized(29) an 80 ns all-atom explicit solvent simulation of EcNikR starting from the AT state (PDB code 1Q5V). In that work, a potential

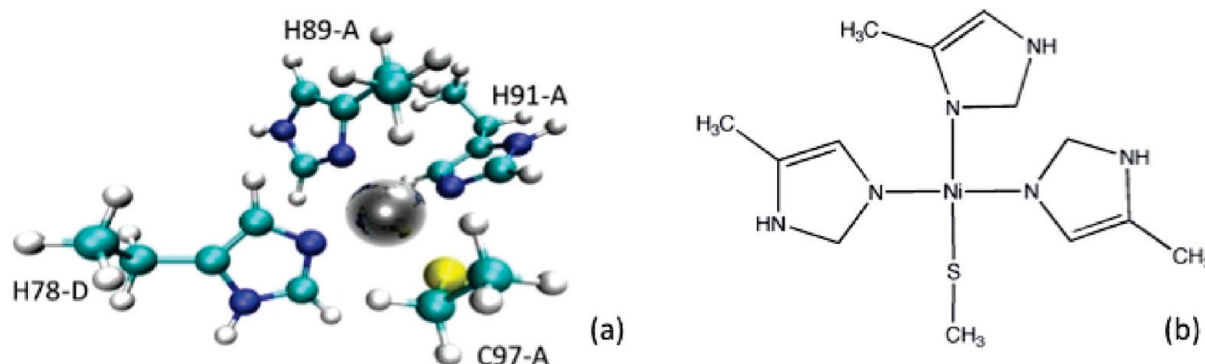


FIGURE 3: Representations of the “small” metal cluster. Atoms included in this model were used to obtain force constants via DFT calculations. (a) A ball-and-stick representation. Labels indicate residue identity and chain ID (b) A 2D representation.

interaction network between the metal-binding and DNA binding residues was highlighted using a novel correlation-matrix-based residue clustering technique (29). However, the metal binding states we not examined. During the preparation of this manuscript, a computational study by Phillips et al. was published regarding NikR metal binding specificity based on free energy simulations (30). This study utilized relatively stable, DNA-bound states of EcNikR for Poisson–Boltzmann thermodynamic integration calculation of free energy differences between different bound ions.

Herein, we examine the dynamics of three 100 ns simulations beginning from three forms of PhNikR in solution. The Ph species was chosen because the crystal structures available had the least amount of missing atoms. We chose the AS, HT (with only four nickels bound), and AT forms (PDB codes: 2BJ3, 2BJ7 (with four primary nickel ions), 2BJ7 (without nickel ions)). Our goal is to highlight the features of the dynamics of each form to compare and contrast any apparent differences between them. The analyses reported herein include rmsd analysis to look at conformational changes of various regions of interest, center-of-mass angular analysis to measure global conformational change, correlation analysis to examine inter-residue communication, and flexibility analysis to identify residues necessary for hinge-motion.

MATERIALS AND METHODS

Simulation Details. We chose to simulate three forms of PhNikR(22): the apo-straight form, taken from PDB ID 2BJ3 (PhNikR-AS), the holo-trans form with only four nickels simulated, taken from PDB ID 2BJ7 (PhNikR-HT), and an apo-trans from where all nickels were stripped from the original pdb structure 2BJ7 (PhNikR-AT). An implicit generalized Born solvation model (GB(OBC))(31) was chosen to reduce the system size as well as the solvent viscosity to allow for faster kinetics (32). Recently, Hornak et al. successfully utilized implicit solvation to witness flap-motion in a simulation of HIV-1 protease (33, 34). In our simulations, each form was taken from the appropriate PDB structure with missing residues built by the TLEAP program, which is part of the AMBER suite (35). The PhNikR-HT form required additional modeling in order to properly represent the nickel centers (see the Force Field Parameters section). The proteins were simulated in AMBER using the ff99SB parameter set (36). Hydrogen vibrations were restrained using the SHAKE algorithm allowing a 2 fs time step. Each form was minimized in AMBER10 using the SANDER module, then relaxed at 100 K for 10 ps. The production runs were 100 ns long at 300 K for each

form using the PMEMD module. Temperature was regulated by utilization of Langevin dynamics using a 1.0 ps^{-1} solvent coupling constant. Successive restart runs utilized different pseudorandom seeds as recommended by Sindhikara et al. (37). Analysis of the trajectories was performed using the PTRAJ module.

Force Field Parameters. All 138×4 of the amino acid residues in Ph apo-NikR occur naturally, and thus force field parameters are available in various parameter sets (ff99SB in our case(36)). For the apo forms, all histidine protonation states were chosen to agree with the most likely protonation state at the experimental pH of 7.5 and are thus delta-protonated. Since in the apo form no histidines are hydrogen bound any other residues, the difference between the delta and epsilon (the second most likely state) protonation will have a limited impact, if at all, to global dynamics.

For the nickel-bound form, there are several approaches to metal modeling that we could have chosen. These approaches can roughly be classified into three categories: quantum mechanical, nonbonded, and bonded. Quantum mechanical treatment or a mixed QM/MM treatment of metals has the most potential for accuracy, but its huge computational cost deters usage for large systems. A nonbonded approach would treat the nickel as a free ion whose interaction with the protein is strictly through van der Waals and Coulomb forces. This is the approach Phillips et al. in their metal preference study (30). This approach is delicate to parametrize, does not enforce a particular geometry, and may ignore any covalent bond characteristics (38–42). Finally, a bonded approach utilizes all terms in the typical all-atom force field to treat the metal ion. Parameterization of this approach can be done by combination of experimental and quantum mechanical methods. This method is the most restrictive geometrically, but is useful when modeling stable metal sites. We chose the bonded approach since NikR is too large to treat quantum mechanically, and we know precisely what the Ni coordination state is in NikR.

New force field parameters were created and used for both the bound nickel ions, and the ligating residues. The MTK++ package was used to expedite the force field parametrization process (43). First, a single copy of one of the nickels plus the four ligating side chains were isolated from the holo structure (pdb code: 2BJ7) then capped with CH₃ groups (in the position of the original). Figure 3a,b show representations of this “small” metal-cluster model.

The histidine protonation states were taken from experiment: H91-A and H78-D are epsilon-protonated, and H89-A is delta-protonated with the remaining sites occupied by the nickel ion.

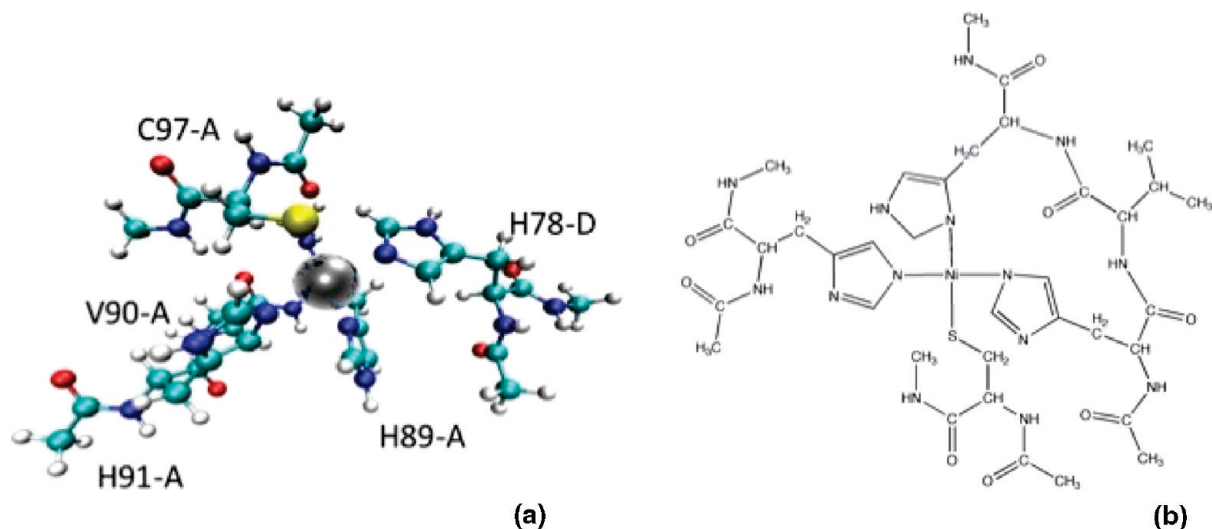


FIGURE 4: Representations of the “large” metal cluster. Atoms included in this model were used to obtain partial atomic charges via DFT. (a) A ball-and-stick representation. (b) A 2D representation.

Table 1: Classification of Structure Based on Angles between Centers of Mass of Different Domains

	angle ($\text{DBD}_{\text{AB}}, \text{MBD}_{\text{AB}}, \text{MBD}_{\text{CD}}$)	angle ($\text{MBD}_{\text{AB}}, \text{MBD}_{\text{CD}}, \text{DBD}_{\text{CD}}$)	dihedral ($\text{DBD}_{\text{AB}}, \text{MBD}_{\text{AB}}, \text{MBD}_{\text{CD}}, \text{DBD}_{\text{CD}}$)
straight	$\approx 180^\circ$	$\approx 180^\circ$	any
cis	$< 180^\circ, > 90^\circ$	$< 180^\circ, > 90^\circ$	$\approx 0^\circ$
trans	$< 180^\circ, > 90^\circ$	$< 180^\circ, > 90^\circ$	$\approx 180^\circ$

The resultant cluster was then minimized using the TPSSTPSS/TZVP level of DFT theory with Gaussian 03 (44). This method and basis has been shown to model nickel compounds well (45). The minimization did not alter the square-planar geometry (though use of smaller basis sets did, data not shown). Following the minimization, force constant calculations were performed using the same methods.

To obtain the partial charges on all the atoms, a larger cluster was selected from the pdb file, this time including backbone atoms, but capped with acetyl and N-methyl groups in appropriate positions. Figure 4a,b shows representations of this “large” cluster.

Charges were obtained using the RESP algorithm(46–53) on this model cluster. van der Waals parameters were not adjusted for the ligating residues. For the nickel, thermodynamic-integration simulations were performed for $\text{Ni}^{2+} + 2\text{Cl}^- + n\text{H}_2\text{O} \rightarrow n\text{H}_2\text{O}$ for various ϵ and r values for nickel. The combination of r and ϵ that most closely resulted in the experimental free energy of hydration was used for nickel (54). The new set of parameters for the nickel ions and ligating residues were then mapped to the four primary nickel-binding sites in the holo form of NikR. The ff99SB parameter set(36) was used for all other residues. Note that although no restraints were used to maintain the planarity of the nickel center the planarity was maintained throughout the course of the simulations described below (data not shown).

Table 1 shows the partial charges of the nickel center along with those of the nickel-bound atoms. For the nickel ion, we used a van der Waals radius of 1.10 Å and a well-depth of 0.013 kcal/mol in all instances. All additional parameters are available in the Supporting Information.

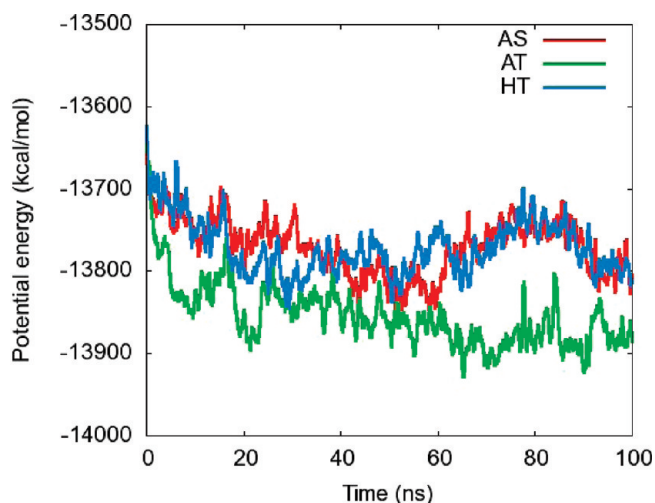


FIGURE 5: Averaged potential energy time series for three simulations of NikR. The smoothing window size is 50 ps.

RESULTS AND DISCUSSION

Simulation Stability. To evaluate the energetic relaxation of the simulations, the potential energy of each system was examined. Figure 5 shows a block-averaged time-series of the potential energy. AS refers to the straight nickel-free structure (pdb ID 2BJ3), AT the trans nickel-free structure (pdb ID 2BJ7), and HT is the nickel-bound trans structure (pdb ID 2BJ7).

The potential energy for all simulations had standard deviations below 80 kcal/mol for the last 90% of the simulation. This is consistent with the fluctuation in the simulation by Bradley et al. (29) whose potential energy fluctuated by about 200 kcal/mol. It should be noted, however, that these systems’ potential landscapes are quite different considering the different solvent representations. The potential energy drops off slightly for the first 10 ns. After that, all three simulations fluctuate about each of their respective averages. Thus, for the final 90 ns, each simulation is likely in thermal equilibrium.

Global Conformational Dynamics. Observing the global rmsd vs time can give a first glimpse as to whether major conformational changes occurred during the simulation. A relatively static rmsd compared to the initial structure suggests

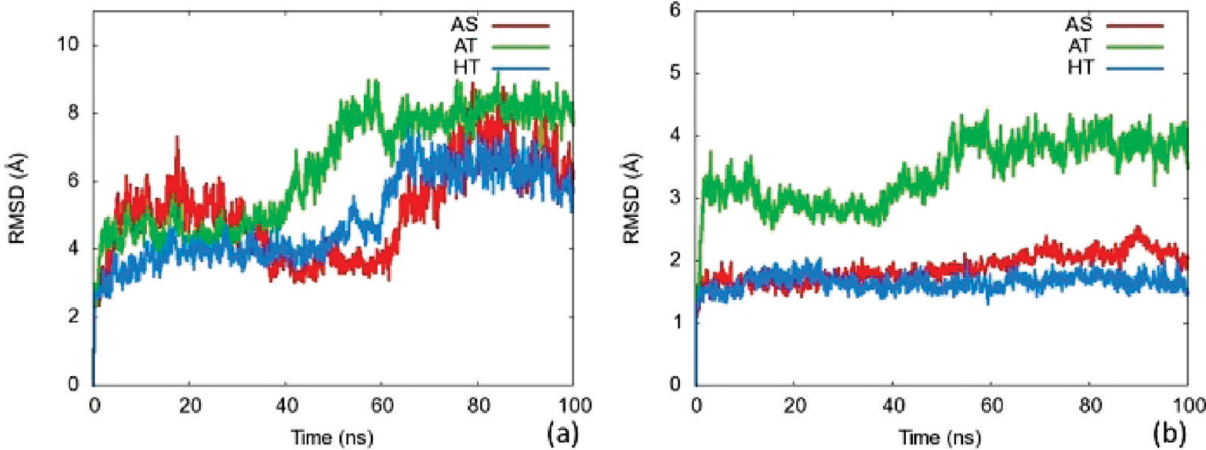


FIGURE 6: rmsd plots for C α atoms of selected regions of NikR. (a) C α rmsd for entire protein in the AS, AT, and HS simulations, (b) C α rmsd for the metal binding domain for all three simulations.

a stable conformation, while a dynamic rmsd suggests significant motion (though it gives little insight to the specifics of that motion). Figure 6a,b shows the rmsd of C α atoms for key subsets of the NikR structure. Figure 6a shows the C α rmsd against the initial structure versus time for all three simulations (AS, AT, and HT). All three simulations deviate more than 2 Å within the first nanosecond. Though none of the simulations are stable over the entire 100 ns of simulation, they each maintain a steady rmsd between transitions. Both of the simulations whose initial structures came from forms found via crystallography (AS and HT) maintain states for nearly 60 ns. The AT simulation only stays steady for ~40 ns and experiences the highest rmsd change. The magnitude of fluctuations is similar to that of the 80 ns explicit solvent *E. coli* simulation of Bradley et al. (29) whose backbone rmsd, after relaxation, fluctuated between 2.5 and 5 Å. The greater fluctuation observed in the simulations herein is likely due to the lack of explicit solvent molecules in the GB simulation. This inhomogeneous behavior suggests that none of the three systems have attained conformational equilibrium within the limit of the 100 ns time scale used in our simulations. Thus, we conclude that our analyses of the resultant trajectories only provide qualitative insights into these fascinating systems.

The X-ray structures available for NikR suggest that the central MBD and two flanking DBDs may act similarly to rigid bodies. If each of these domains were rigid, the C α rmsd would be relatively low and stable throughout the simulation. Figure 4b shows the C α rmsd against the first frame for only the MBD of the protein (residues 57–131 of each chain). Both the AS and HT simulations jump initially and stay in a steady state between 1.5 and 2 Å from the initial structure. Thus, for these two forms, the central MBD is relatively rigid throughout the simulation. For the AS and HT forms, the large conformational change around 60 ns indicated by the full protein rmsd in Figure 6a must not be directly due to changes within the MBD. The AT simulation jumps initially to 3 Å then rises to 4 Å between the 40th and 60th ns. This larger jump may be due to the instability of the initial nickel-free AT structure and may be the source of the global conformational change indicated in Figure 6a. Since the MBD is relatively stable for both the AS and HT simulations, the conformational changes must come from the DBD motion. rmsd plots for DBDs can be found in the Supporting Information.

To observe the rigid body motion of the DBDs relative to the MBD, motion was observed in the context of the transition between the straight, trans, and cis forms referred to in Figure 2.

Table 2: Partial Charges for the Nickel Center along with Each Ligating Atom^a

Ni ²⁺	Cys 97 S	H89 NE (HID)	H91 ND (HIE)	H78D NE (HID)
0.66275	−0.52432	−0.66101	0.00690	−0.16857

^aPartial charges for each atom in the ligating residues are provided in the Supporting Information.

Consider the centers of mass (COMs) of the four major domains: DBD from chains A and B (DBDAB), MBD from AB (MBDAB), MBD from CD (MBDCD), and DBD from CD (DBDCD). We can classify the shape of the protein based on these four points as in Table 2.

Figure 7a,b shows the angles between both (DBDAB, MBDAB, and MBDCD) and (MBDAB, MBDCD, and DBDCD) for all three forms. The AS form clearly maintains angles near 180 degrees, indicating that the COMs of the four domains are roughly linear. Conversely, the AT and HT forms maintain an angle of 150 degrees or less — indicating a bend in the structure. While fluctuations do exist, no major conformational changes are evident from this analysis other than the HT CD DBD, which drifts near 160 degrees. This could indicate that this DBD is “straightening out”. Interestingly, the flapping motion seems to be independent, suggesting that the global conformational rearrangement may act in a stepwise fashion, rather than in concert.

Figure 7c shows the dihedral angle between these four points for each simulation. Unsurprisingly, the AS domain–COM dihedral angle fluctuates wildly across all angles since it is nearly linear and thus small motions can cause large angular changes. Conversely, the AT and HT, both starting at less than −150°, slowly drift up throughout the simulation. This could be simply relaxation, or more significantly, a slow conformational change to the cis form.

These C α rmsd and domain COM angular analyses indicate significant conformational motion, but no complete transitions between the major states observed in the crystallographic experiments. However, the CD DBD of the HT simulation begins to straighten out within the time scale of the simulation. This motion suggests that conformational transitions may be observable within an order of magnitude longer simulation (~1 μ s).

Features of Key Structural Segments. Though the relative motion of the large domains reflects global conformational

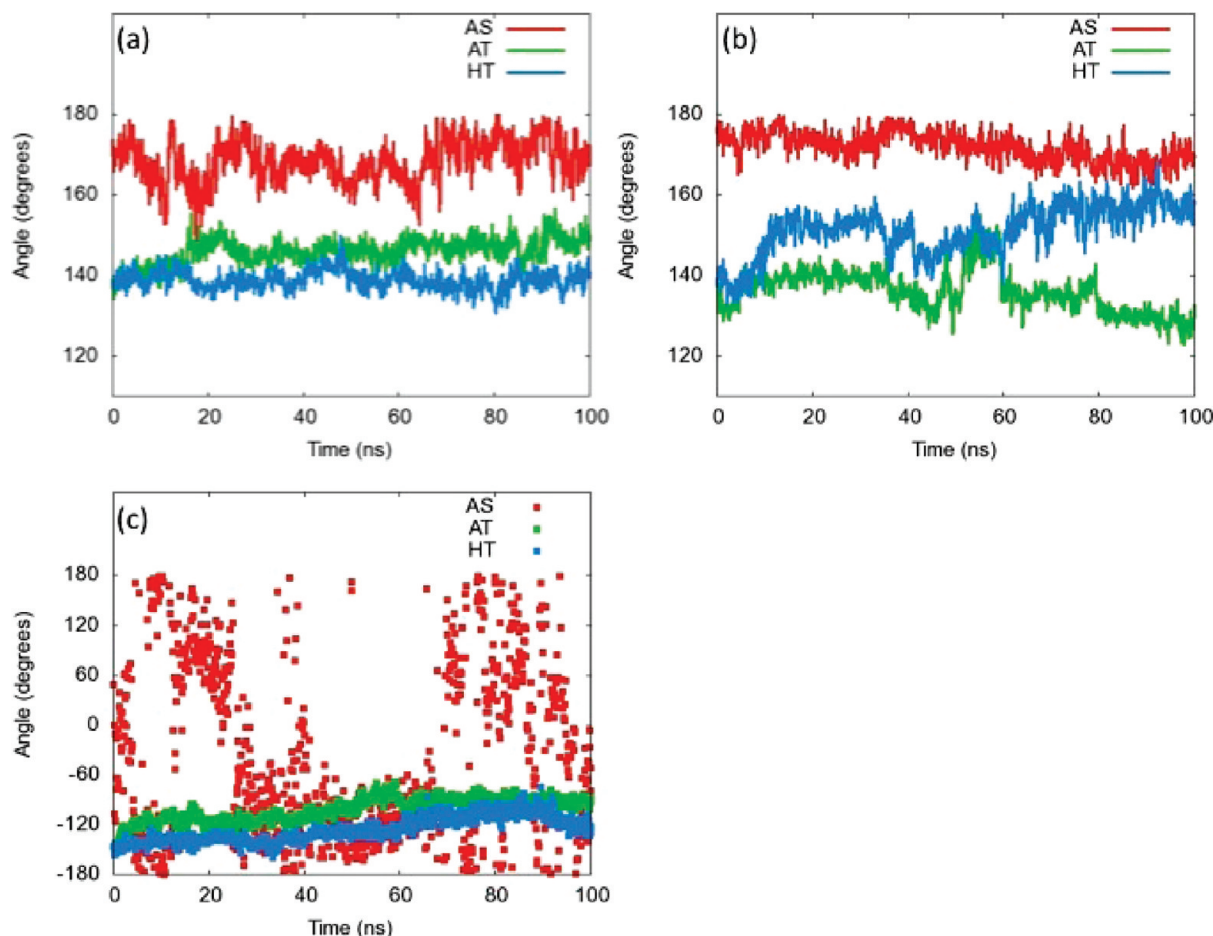


FIGURE 7: Angles between centers of mass of adjacent domains vs time. (a) Angle made by DBDAB, MBDAB, and MBDCD. (b) Angle made by MBDAB, MBDCD, and DBDCD. (c) Dihedral angle between DBDAB, MBDAB, MBDCD, and DBDCD.

changes, the behavior of the segments that comprise and connect these regions can reflect the communication between them. We identified structural segments with key functionalities by analyzing both residue-level distance correlation and flexibility.

(A). *Residue Correlation.* To elucidate inter-residue dynamical relationships, distance correlation analysis was performed on all C α atoms for each simulation with the PTRAJ module from AMBER10 (see eq 1).

$$C(i,j) = \frac{\langle \Delta x_i(t_k) \cdot \Delta x_j(t_k) \rangle}{\langle \Delta x_i(t_k)^2 \rangle^{1/2} \langle \Delta x_j(t_k)^2 \rangle^{1/2}} \quad (1)$$

The correlation matrices for each simulation (found in SM) contain much information but are difficult to parse visually. Bradley et al. reported visually similar correlation plots for their EcNikR simulation. In order to quantify the relevance of specific residues, we summed the absolute value of the correlation matrix along either a row or column for each residue summed over the four chains as in eq 2.

$$cREL_i = \sum_{chains} \sum_{j=1}^M |c_{i,j}| \quad (2)$$

Here M is the number of residues per chain. Figure 8a shows this correlation relevance summed over chains (cREL). The colored area just above the x -axis indicates biological information including binding residues and highly conserved residues across 12 selected species of NikR (55–65). We chose to use the same 12 species examined in the original PhNikR crystal

structure paper by Chivers et al.(22) The DNA binding residues include those involved in nonspecific contacts. The graphs suggest that each form exhibits similar behavior, residue-to-residue, and that the residues of AS and HT forms are much more coupled. Interestingly, for most of the DBD (approximately first 38 residues) for these two forms, the chain-independent correlation relevance values are nearly identical. In the MBD, the AS is more correlated than the HT form (and even more so than the AT). Additionally, the graph suggests that residues with known biological function tend to have higher correlation relevance with the exception of Gly-67, which may require more flexibility.

Figure 8b shows the values cREL of the HT simulation (though all simulations are qualitatively similar in this respect) applied to a color scheme (red is the highest, blue is the lowest). Remarkably, both the segments of secondary structure involved in nickel-binding ($\alpha 3$ and $\beta 3$) and those involved in DNA-binding ($\beta 1$) have the highest value of cREL. This suggests that these regions are the most important structural regions since they coordinate motion the strongest with other residues. Mutation of the residues that would disrupt the structural stability of these segments would likely inhibit DNA-binding. Previously performed mutation studies of some of the residues for various species in these segments have already shown the importance of these segments in DNA and nickel-binding (13, 18, 21). However, the DNA binding characteristics of each species is unique; thus, mutation studies should be performed on different but analogous residues. Additional correlation analysis can be found in the SM.

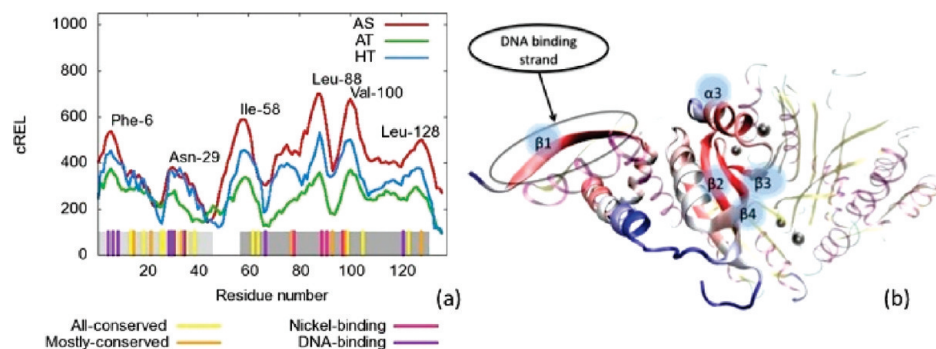


FIGURE 8: Correlation relevance summed over chains (cREL) for all three simulations. (a) cREL vs residue number. Residue identities are labeled at peak values. Bottom bars indicate residues with high conservation across species, or with either nickel or DNA binding function as labeled. Light and dark gray regions represent the DBD and MBD, respectively. (b) Correlation relevance summed over chains (cREL) for the HT simulation applied to a color scheme (red is the highest, blue is the lowest) on a single chain the initial structure of the HT form of NikR. The rest of the protein is present but deemphasized and uses the same color scheme as Figure 1. The figure suggests a strong influence on the rest of the protein by the secondary structure segments involved in both DNA and nickel binding.

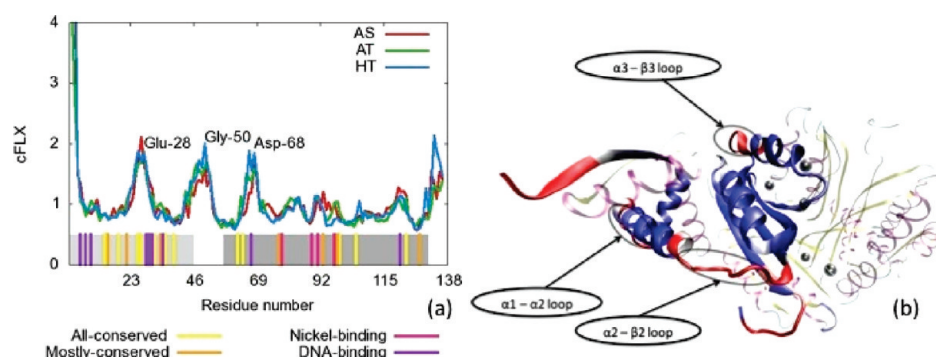


FIGURE 9: Residue flexibility, cFLX, for all three simulations. (a) cFLX vs residue number. Residue identities are labeled at peak values. Bottom bars indicate residues with high conservation across species, or with either nickel or DNA binding function as labeled. Light and dark gray regions represent the DBD and MBD respectively. (b) Flexibility summed over chains (cFLX) for the HT simulation applied to a color scheme (red is the highest, blue is the lowest) on a single chain the initial structure of the HT form of NikR. The rest of the protein is present but deemphasized and uses the same color scheme as Figure 1. Highly flexible regions may be key for functional conformational changes.

We note that Bradley et al. utilized a different correlation-based measure to determine interaction groups rather than individual residue relevance as shown here (29).

(B). *Residue Flexibility*. Flexibility can be a necessary attribute in key regions of a protein to allow it to not only fold but also undergo functional conformational changes. For example, flexibility in hinge regions is advantageous (66–68). To identify regions of high flexibility in NikR, each residue was characterized by the standard deviation of the distance between the C α atoms of its nearest neighbors summed over chains (see eq 3).

$$cFLX_i = \sum_{\text{chains}} \sigma(|\vec{x}_{i-1} - \vec{x}_{i+1}|) \quad (3)$$

Here \vec{x}_i represents the position of the C α atom of the i th residue. Figure 9a shows cFLX for each simulation. The flexibility seems to be almost identical for all three simulations suggesting the form has little effect on the residue-level motion. High flexibility is seen at the two termini as well as in three regions centered on Glu-28, Gly-50, and Asp-68 as labeled. It is unsurprising that the correlation relevance, cREL, and flexibility, cFLX, do not correlate with each other. cREL corresponds more to structural stability, while cFLX corresponds to instability. We note that there is no correlation between the X-ray B-factor and this measure of flexibility (data not shown). This loop flexibility may play a key role in allowing the allosteric conformational

change required for NikR's function. A mutation to a residue within a region of high flexibility to increase stability should decrease the biological function.

Figure 9b shows the values cFLX of the HT simulation in the same manner as in 8b applied to a color scheme (red is the highest, blue is the lowest). The figure shows that the highest flexibility regions are in only a few of the loop regions, particularly the $\alpha 1$ - $\alpha 2$, $\alpha 2$ - $\beta 2$, and $\alpha 3$ - $\beta 3$ loops (these correspond to the three peaks in Figure 9a). The analogous flexible loops for *E. coli* are Gly-24 to Asn-27, Gln-47 to Gln-51 and Glu-70 to Asp-73, and for *H. pylori* are Gly-33 to Ser-36, Glu-56 to Asn-60, and His-72 to Glu-85. While all three of these loop regions may have a distinct biological function, the $\alpha 2$ - $\beta 2$ loop is the most interesting in the context of the global conformational changes NikR undergoes since it lies at the interface between the DBD and MBD regions. The hinge-motion of this loop is key for the switching between the cis, trans, and straight conformations. Interestingly, the sequence conservation in this region is low (55–65). This may indicate that these residues are necessary in DNA-binding specificity.

Since the $\alpha 2$ - $\beta 2$ loop is a hinge that allows the global conformational change required for NikR to bind to DNA (converting to the cis-form), and in the wild type it is highly flexible, mutations to this region that restrict motion should inhibit DNA binding activity. Two key features of this loop are highlighted in Figure 10. The first is the Gly-50 residue that most known species of NikR contain (it is absent in the $\alpha 2$ - $\beta 2$ loop of

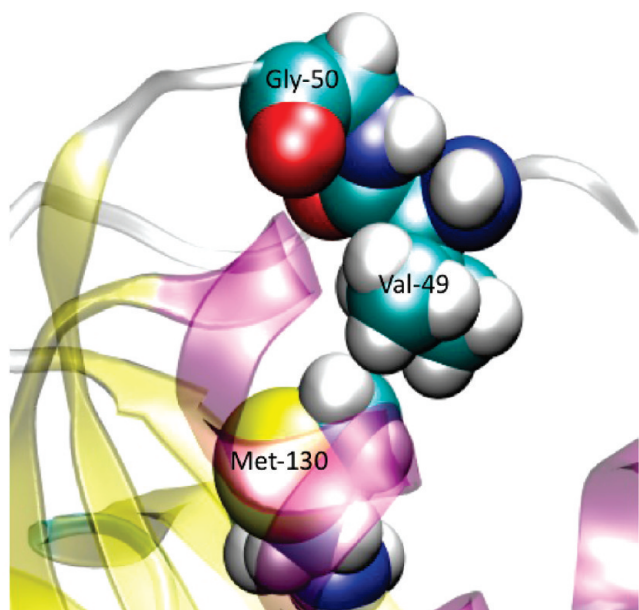


FIGURE 10: Close-up of $\alpha 2$ - $\beta 2$ loop. Key residues are represented by VDW volume spheres and labeled appropriately. Gly-50 provides flexibility. Shortening the side chains while keeping the hydrophobic interaction can reduce the $C\alpha$ - $C\alpha$ distance between residues 49 and 130.

H. pylori) (55–65). The mutation of this glycine to a conformationally less flexible residue such as a proline might reduce NikR's ability to change conformation to accommodate DNA binding. Second, there is a hydrophobic interaction between Val-49 in the $\alpha 2$ - $\beta 2$ loop and Met-1 in the $\beta 5$ strand. The reduction of the length of either of these side chains could reduce the flexibility as well. For example, mutation of the Met-1 to a Val or Val-49 to Ala would keep the hydrophobic interaction but would tie-down the loop to restrict motion. Similar mutations on other species of NikR would likely produce the same effect. For example, in HpNikR, this interaction is Coulombic rather than hydrophobic (Lys-31 with Glu-56) as the crystal structure (PDBID: 2CA9) suggests. For *E. coli*, the interactions are not obvious from the crystal structure (PDBID: 2HZA); however, the study by Bradley et al. did indeed recognize a noncovalent interaction in this general region (in that a unified cluster was recognized containing both sides of this region).

CONCLUSIONS

NikR regulates cellular nickel concentration by responding to high nickel concentrations by suppressing nickel transport protein expression. Experimental data give clues to its mechanism but without conclusive detail. We have performed three simulations to help elucidate the dynamics of NikR. The modeling of this system required special parametrization to accurately represent the nickel and its ligating residues. Our analyses of these simulations provide additional insight into the dynamical preference that different initial conformations and nickel-binding states have on the protein. While not observing global conformational changes on the computational time-scale available, several distinct features of NikR were observed. The flanking DBDs move independently of each other. Analysis of biologically relevant residues tend to influence motion across domains much more strongly than other residues.

The secondary structure segments directly pertaining to binding of either DNA or nickel were found to be structurally

important by correlation analysis even in the absence of both of these ligands. Additionally, key flexible regions were highlighted especially the $\alpha 2$ - $\beta 2$ loop whose hinge-like motion allows functional global conformational change. Regions with either high correlation relevance or flexibility seem to be correlated with biologically important regions. We suggested some specific mutations to these residues for the *P. horikoshii* species and also identified analogous regions in *E. coli* and *H. pylori* species of NikR that we expect to have similar character.

With current computational capacity, simulating a global conformational change in a system such as NikR is a significant challenge. Beyond brute force simulations, it is possible that advanced sampling algorithms could be applied to not only establish a meaningful reaction coordinate between NikR states, but also to calculate the free-energy change between states.

ACKNOWLEDGMENT

We thank Martin B. Peters for assistance with the metal modeling software (MTK++). We also thank the anonymous reviewer for excellent and thorough reviews and suggestions.

SUPPORTING INFORMATION AVAILABLE

Additional rmsd plots, correlation plots, fluctuation analysis, as well as force field parameters. This material is available free of charge via the Internet at <http://pubs.acs.org>.

REFERENCES

- Culotta, V. C., Yang, M., and O'Halloran, T. V. (2006) Activation of superoxide dismutases: Putting the metal to the pedal. *Biochim. Biophys. Acta - Mol. Cell Res.* 1763 (7), 747–758.
- Finney, L. A., and O'Halloran, T. V. (2003) Transition metal speciation in the cell: insights from the chemistry of metal ion receptors. *Science* 300 (5621), 931–937.
- Dosanjh, N. S., and Michel, S. L. J. (2006) Microbial nickel metallo-regulation: NikRs for nickel ions. *Curr. Opin. Chem. Biol.* 10 (2), 123–130.
- Valentine, J. S., Doucette, P. A., and Potter, S. Z. (2005) Copper-zinc superoxide dismutase and amyotrophic lateral sclerosis. *Annu. Rev. Biochem.* 74, 563–593.
- Rosenzweig, A. C. (2001) Copper delivery by metallochaperone proteins. *Acc. Chem. Res.* 34 (2), 119–128.
- Gaggelli, E., Kozlowski, H., Valensin, D., and Valensin, G. (2006) Copper homeostasis and neurodegenerative disorders (Alzheimer's, prion, and Parkinson's diseases and amyotrophic lateral sclerosis). *Chem. Rev.* 106 (6), 1995–2044.
- Beckman, J. S.; Estevez, A. G.; Crow, J. P.; Barbeito, L. (2001) Superoxide dismutase and the death of motoneurons in ALS. *Trends Neurosci.* 24 (11 Suppl), S15–20.
- Huffman, D. L., and O'Halloran, T. V. (2001) Function, structure, and mechanism of intracellular copper trafficking proteins. *Annu. Rev. Biochem.* 70, 677–701.
- Maroney, M. J. (1999) Structure/function relationships in nickel metallobiochemistry. *Curr. Opin. Chem. Biol.* 3 (2), 188–199.
- Mulrooney, S. B., and Hausinger, R. P. (2003) Nickel uptake and utilization by microorganisms. *FEMS Microbiol. Rev.* 27 (2–3), 239–261.
- Mobley, H. L. T., and Hausinger, R. P. (1989) Microbial ureases - significance, regulation, and molecular characterization. *Microbiol. Rev.* 53 (1), 85–108.
- De Pina, K., Desjardin, V., Mandrand-Berthelot, M. A., Giordano, G., and Wu, L. F. (1999) Isolation and characterization of the nikR gene encoding a nickel-responsive regulator in *Escherichia coli*. *J. Bacteriol.* 181 (2), 670–674.
- Chivers, P. T., and Sauer, R. T. (1999) NikR is a ribbon-helix-helix DNA-binding protein. *Protein Sci.* 8 (11), 2494–2500.
- Chivers, P. T., and Sauer, R. T. (2000) Regulation of high affinity nickel uptake in bacteria. Ni^{2+} -Dependent interaction of NikR with wild-type and mutant operator sites. *J. Biol. Chem.* 275 (26), 19735–19741.

15. Contreras, M., Thiberge, J. M., Mandrand-Berthelot, M. A., and Labigne, A. (2003) Characterization of the roles of NikR, a nickel-responsive pleiotropic autoregulator of *Helicobacter pylori*. *Mol. Microbiol.* 49 (4), 947–963.
16. Chivers, P. T., and Sauer, R. T. (2002) NikR repressor: High-affinity nickel binding to the C-terminal domain regulates binding to operator DNA. *Chem. Biol.* 9 (10), 1141–1148.
17. Bloom, S. L., and Zamble, D. B. (2004) Metal-selective DNA-binding response of *Escherichia coli* NikR. *Biochemistry* 43 (31), 10029–38.
18. Carrington, P. E., Chivers, P. T., Al-Mjeni, F., Sauer, R. T., and Maroney, M. J. (2003) Nickel coordination is regulated by the DNA-bound state of NikR. *Nat. Struct. Biol.* 10 (2), 126–130.
19. Schreiter, E. R., Sintchak, M. D., Guo, Y. Y., Chivers, P. T., Sauer, R. T., and Drennan, C. L. (2003) Crystal structure of the nickel-responsive transcription factor NikR. *Nat. Struct. Biol.* 10 (10), 794–799.
20. Schreiter, E. R., Wang, S. C., Zamble, D. B., and Drennan, C. L. (2006) NikR-operator complex structure and the mechanism of repressor activation by metal ions. *Proc. Natl. Acad. Sci. U. S. A.* 103 (37), 13676–13681.
21. Dian, C., Schauer, K., Kapp, U., McSweeney, S. M., Labigne, A., and Terradot, L. (2006) Structural basis of the nickel response in *Helicobacter pylori*: Crystal structures of HpNikR in Apo and nickel-bound states. *J. Mol. Biol.* 361 (4), 715–730.
22. Chivers, P. T., and Tahirov, T. H. (2005) Structure of *Pyrococcus horikoshii* NikR: Nickel sensing and implications for the regulation of DNA recognition. *J. Mol. Biol.* 348 (3), 597–607.
23. Schreiter, E. R., Chivers, P. T., and Drennan, C. L. (2004) Crystal structures of the Ni-dependent transcriptional repressor NikR from *E. coli*. *FASEB J* 18 (8), C188–C188.
24. Phillips, C. M., Schreiter, E. R., Guo, Y., Wang, S. C., Zamble, D. B., and Drennan, C. L. (2008) Structural basis of the metal specificity for nickel regulatory protein NikR. *Biochemistry* 47 (7), 1938–1946.
25. Zambelli, B., Bellucci, M., Danielli, A., Scarlato, V., and Ciurli, S. (2007) The Ni²⁺ binding properties of *Helicobacter pylori* NikR. *Chem. Commun.* 35, 3649–3651.
26. Koshland, D. E., Nemethy, G., and Filmer, D. (1966) Comparison of experimental binding data and theoretical models in proteins containing subunits. *Biochemistry* 5 (1), 365–385.
27. Karplus, M., and McCammon, J. A. (2002) Molecular dynamics simulations of biomolecules. *Nat. Struct. Biol.* 9 (9), 646–652.
28. Cui, G., and Merz, K. M. (2008) The intrinsic dynamics and function of nickel-binding regulatory protein: Insights from elastic network analysis. *Biophys. J.* 94 (10), 3769–3778.
29. Bradley, M. J., Chivers, P. T., and Baker, N. A. (2008) Molecular dynamics simulation of the *Escherichia coli* NikR protein: Equilibrium conformational fluctuations reveal interdomain allosteric communication pathways. *J. Mol. Biol.* 378 (5), 1155–1173.
30. Phillips, C. M., Nerenberg, P. S., Drennan, C. L., and Stultz, C. M. (2009) Physical basis of metal-binding specificity in *Escherichia coli* NikR. *J. Am. Chem. Soc.* 131 (29), 10220–10228.
31. Onufriev, A., Bashford, D., and Case, D. A. (2004) Exploring protein native states and large-scale conformational changes with a modified generalized born model. *Proteins: Struct., Funct., Bioinf* 55 (2), 383–394.
32. Zagrovic, B., and Pande, V. (2003) Solvent viscosity dependence of the folding rate of a small protein: Distributed computing study. *J. Comput. Chem.* 24 (12), 1432–1436.
33. Hornak, V., Okur, A., Rizzo, R. C., and Simmerling, C. (2006) HIV-1 protease flaps spontaneously close to the correct structure in simulations following manual placement of an inhibitor into the open state. *J. Am. Chem. Soc.* 128 (9), 2812–2813.
34. Hornak, V., Okur, A., Rizzo, R. C., and Simmerling, C. (2006) HIV-1 protease flaps spontaneously open and reclose in molecular dynamics simulations. *Proc. Natl. Acad. Sci. U. S. A.* 103 (4), 915–920.
35. Case, D. A., Cheatham, T. E., Darden, T., Gohlke, H., Luo, R., Merz, K. M., Onufriev, A., Simmerling, C., Wang, B., and Woods, R. J. (2005) The Amber biomolecular simulation programs. *J. Comput. Chem.* 26 (16), 1668–1688.
36. Hornak, V., Abel, R., Okur, A., Strockbine, B., Roitberg, A., and Simmerling, C. (2006) Comparison of multiple amber force fields and development of improved protein backbone parameters. *Proteins: Struct., Funct., Bioinf.* 65 (3), 712–725.
37. Sindhikara, D. J., Kim, S., Voter, A. F., and Roitberg, A. E. (2009) Bad seeds sprout perilous dynamics: Stochastic thermostat induced trajectory synchronization in biomolecules. *J. Chem. Theory Comput.* 5 (6), 1624–1631.
38. Stote, R. H., and Karplus, M. (1995) Zinc-binding in proteins and solution - a simple but accurate nonbonded representation. *Proteins: Struct., Funct., Genet.* 23 (1), 12–31.
39. Sakharov, D. V., and Lim, C. (2005) Zn protein simulations including charge transfer and local polarization effects. *J. Am. Chem. Soc.* 127 (13), 4921–4929.
40. Aqvist, J., and Warshel, a. (1992) Computer-simulation of the initial proton-transfer step in human carbonic anhydrase-I. *J. Mol. Biol.* 224 (1), 7–14.
41. Pang, Y. P. (2001) Successful molecular dynamics simulation of two zinc complexes bridged by a hydroxide in phosphotriesterase using the cationic dummy atom method. *Proteins: Struct., Funct., Genet.* 45 (3), 183–189.
42. Pang, Y. P., Xu, K., El Yazal, J., and Prendergast, F. G. (2000) Successful molecular dynamics simulation of the zinc-bound farnesyltransferase using the cationic dummy atom approach. *Protein Sci.* 9 (10), 1857–1865.
43. Peters, M. MTK++ Website. <http://www.qtp.ufl.edu/~peters/MTKpp/index.html>.
44. Frisch, M. J.; Trucks, G. W.; Schlegel, H. B.; Scuseria, G. E.; Robb, M. A.; Cheeseman, J. R.; Montgomery, J. A., Jr.; Vreven, T.; Kudin, K. N.; Burant, J. C.; Millam, J. M.; Iyengar, S. S.; Tomasi, J.; Barone, V.; Mennucci, B.; Cossi, M.; Scalmani, G.; Rega, N.; Paterson, G. A.; Nakatsuji, H.; Hada, M.; Ehara, M.; Toyota, K.; Fukuda, R.; Hasegawa, J.; Ishida, M.; Nakajima, T.; Honda, Y.; Kitao, O.; Nakai, H.; Klene, M.; Li, X.; Knox, J. E.; Hratchian, H. P.; Cross, J. B.; Bakken, V.; Adamo, C.; Jaramillo, J.; Gomperts, R.; Stratmann, R. E.; Yazyev, O.; Austin, A. J.; Cammi, R.; Pomelli, C.; Ochterski, J. W.; Ayala, P. Y.; Morokuma, K.; Voth, G. A.; Salvador, P.; Dannenberg, J. J.; Zakrzewski, V. G.; Dapprich, S.; Daniels, A. D.; Strain, M. C.; Farkas, O.; Malick, D. K.; Rabuck, A. D.; Raghavachari, K.; Foresman, J. B.; Ortiz, J. V.; Cui, Q.; Baboul, A. G.; Clifford, S.; Cioslowski, J.; Stefanov, B. B.; Liu, G.; Liashenko, A.; Piskorz, P.; Komaromi, I.; Martin, R. L.; Fox, D. J.; Keith, T.; Al-Laham, M. A.; Peng, C. Y.; Nanayakkara, A.; Challacombe, M.; Gill, P. M. W.; Johnson, B.; Chen, W.; Wong, M. W.; Gonzalez, C.; Pople, J. A. Gaussian 03, C.02; Gaussian Inc.: Wallingford, CT, 2004.
45. Riley, K. E., and Merz, K. M. (2007) Assessment of density functional theory methods for the computation of heats of formation and ionization potentials of systems containing third row transition metals. *J. Phys. Chem. A* 111 (27), 6044–6053.
46. Kannan, K. K.; Ramanadham, M.; Jones, T. A., (1984) Structure, refinement, and function of carbonic-anhydrase isozymes - refinement of human carbonic anhydrase-I. *Ann. N.Y. Acad. Sci.* 429 (Jun), 49–60.
47. Besler, B. H., Merz, K. M. J., and Kollman, P. A. (1990) Atomic charges derived from semiempirical methods. *J. Comput. Chem.* 11 (4), 431–439.
48. Woods, R. J., Khalil, M., Pell, W., Moffat, S. H., and Smith, J. V. H. (1990) Derivation of net atomic charges from molecular electrostatic potentials. *J. Comput. Chem.* 11 (3), 297–310.
49. Chirlian, L. E., and Francel, M. M. (1987) Atomic charges derived from electrostatic potentials: a detailed study. *J. Comput. Chem.* 8 (6), 894–905.
50. Singh, U. C., and Kollman, P. A. (1984) An approach to computing electrostatic charges for molecules. *J. Comput. Chem.* 5 (2), 129–145.
51. Williams, D. E., and Yan, J. M. (1988) Point-charge models for molecules derived from least-squares fitting of the electric potential. *Adv. Atomic Mol. Phys.* 23, 87–130.
52. Cox, S. R., and Williams, D. E. (1981) Representation of the molecular electrostatic potential by a net atomic charge model. *J. Comput. Chem.* 2 (3), 304–323.
53. Bayly, C. A., Cieplak, P., Cornell, W. D., and Kollman, P. A. (1993) A well behaved electrostatic potential based method using charge restraints for deriving atomic charges: the RESP model. *J. Phys. Chem.* 97, 10269–10280.
54. Floris, F. M., Persico, M., Tani, A., and Tomasi, J. (1994) Hydration shell structure of the calcium-ion from simulations with ab-initio effective pair potentials. *Chem. Phys. Lett.* 227 (1–2), 126–132.
55. Bult, C. J., White, O., Olsen, G. J., Zhou, L. X., Fleischmann, R. D., Sutton, G. G., Blake, J. A., FitzGerald, L. M., Clayton, R. A., Gocayne, J. D., Kerlavage, A. R., Dougherty, B. A., Tomb, J. F., Adams, M. D., Reich, C. I., Overbeek, R., Kirkness, E. F., Weinstock, K. G., Merrick, J. M., Glodek, A., Scott, J. L., Geoghagen, N. S. M., Weidman, J. F., Fuhrmann, J. L., Nguyen, D., Utterback, T. R., Kelley, J. M., Peterson, J. D., Sadow, P. W., Hanna, M. C., Cotton, M. D., Roberts, K. M., Hurst, M. A., Kaine, B. P., Borodovsky, M., Klenk, H. P., Fraser, C. M., Smith, H. O., Woese, C. R., and

- Venter, J. C. (1996) Complete genome sequence of the methanogenic archaeon, *Methanococcus jannaschii*. *Science* 273 (5278), 1058–1073.
56. Klenk, H. P., Clayton, R. A., Tomb, J. F., White, O., Nelson, K. E., Ketchum, K. A., Dodson, R. J., Gwinn, M., Hickey, E. K., Peterson, J. D., Richardson, D. L., Kerlavage, A. R., Graham, D. E., Kyrpides, N. C., Fleischmann, R. D., Quackenbush, J., Lee, N. H., Sutton, G. G., Gill, S., Kirkness, E. F., Dougherty, B. A., McKenney, K., Adams, M. D., Loftus, B., Peterson, S., Reich, C. I., McNeil, L. K., Badger, J. H., Glodek, A., Zhou, L. X., Overbeek, R., Gocayne, J. D., Weidman, J. F., McDonald, L., Utterback, T., Cotton, M. D., Spriggs, T., Artiach, P., Kaine, B. P., Sykes, S. M., Sadow, P. W., DAndrea, K. P., Bowman, C., Fujii, C., Garland, S. A., Mason, T. M., Olsen, G. J., Fraser, C. M., Smith, H. O., Woese, C. R., and Venter, J. C. (1997) The complete genome sequence of the hyperthermophilic, sulphate-reducing archaeon *Archaeoglobus fulgidus*. *Nature* 390 (6658), 364–370.
57. Tomb, J. F.; White, O.; Kerlavage, A. R.; Clayton, R. A.; Sutton, G. G.; Fleischmann, R. D.; Ketchum, K. A.; Klenk, H. P.; Gill, S.; Dougherty, B. A.; Nelson, K.; Quackenbush, J.; Zhou, L. X.; Kirkness, E. F.; Peterson, S.; Loftus, B.; Richardson, D.; Dodson, R.; Khalak, H. G.; Glodek, A.; McKenney, K.; Fitzgerald, L. M.; Lee, N.; Adams, M. D.; Hickey, E. K.; Berg, D. E.; Gocayne, J. D.; Utterback, T. R.; Peterson, J. D.; Kelley, J. M.; Cotton, M. D.; Weidman, J. M.; Fujii, C.; Bowman, C.; Watthey, L.; Wallin, E.; Hayes, W. S.; Borodovsky, M.; Karp, P. D.; Smith, H. O.; Fraser, C. M.; Venter, J. C. (1997) The complete genome sequence of the gastric pathogen *Helicobacter pylori* (Vol. 388, p 539, 1997). *Nature*, 389 (6649), 412–412.
58. McClelland, M., Sanderson, K. E., Spieth, J., Clifton, S. W., Latreille, P., Courtney, L., Porwollik, S., Ali, J., Dante, M., Du, F. Y., Hou, S. F., Layman, D., Leonard, S., Nguyen, C., Scott, K., Holmes, A., Grewal, N., Mulvaney, E., Ryan, E., Sun, H., Florea, L., Miller, W., Stoneking, T., Nhan, M., Waterston, R., and Wilson, R. K. (2001) Complete genome sequence of *Salmonella enterica* serovar typhimurium LT2. *Nature* 413 (6858), 852–856.
59. Deppenmeier, U., Johann, A., Hartsch, T., Merkl, R., Schmitz, R. A., Martinez-Arias, R., Henne, A., Wiezer, A., Baumer, S., Jacobi, C., Bruggemann, H., Lienard, T., Christmann, A., Bomeke, M., Steckel, S., Bhattacharyya, A., Lykidis, A., Overbeek, R., Klenk, H. P., Gunsalus, R. P., Fritz, H. J., and Gottschalk, G. (2002) The genome of *Methanosarcina mazei*: Evidence for lateral gene transfer between bacteria and archaea. *J. Mol. Microbiol. Biotechnol.* 4 (4), 453–461.
60. Eisen, J. A., Nelson, K. E., Paulsen, I. T., Heidelberg, J. F., Wu, M., Dodson, R. J., Deboy, R., Gwinn, M. L., Nelson, W. C., Haft, D. H., Hickey, E. K., Peterson, J. D., Durkin, A. S., Kolonay, J. L., Yang, F., Holt, I., Umayam, L. A., Mason, T., Brenner, M., Shea, T. P., Parksey, D., Nierman, W. C., Feldblyum, T. V., Hansen, C. L., Craven, M. B., Radune, D., Vamathevan, J., Khouri, H., White, O., Gruber, T. M., Ketchum, K. A., Venter, J. C., Tettelin, H., Bryant, D. A., and Fraser, C. M. (2002) The complete genome sequence of *Chlorobium tepidum* TLS, a photosynthetic, anaerobic, green-sulfur bacterium. *Proc. Natl. Acad. Sci. U.S.A.* 99 (14), 9509–9514.
61. Galagan, J. E., Nusbaum, C., Roy, A., Endrizzi, M. G., Macdonald, P., FitzHugh, W., Calvo, S., Engels, R., Smirnov, S., Atnoor, D., Brown, A., Allen, N., Naylor, J., Stange-Thomann, N., DeArellano, K., Johnson, R., Linton, L., McEwan, P., McKernan, K., Talamas, J., Tirrell, A., Ye, W. J., Zimmer, A., Barber, R. D., Cann, I., Graham, D. E., Grahame, D. A., Guss, A. M., Hedderich, R., Ingram-Smith, C., Kuettner, H. C., Krzycki, J. A., Leigh, J. A., Li, W. X., Liu, J. F., Mukhopadhyay, B., Reeve, J. N., Smith, K., Springer, T. A., Umayam, L. A., White, O., White, R. H., de Macario, E. C., Ferry, J. G., Jarrell, K. F., Jing, H., Macario, A. J. L., Paulsen, I., Pritchett, M., Sowers, K. R., Swanson, R. V., Zinder, S. H., Lander, E., Metcalf, W. W., and Birren, B. (2002) The genome of *M. acetivorans* reveals extensive metabolic and physiological diversity. *Genome Res.* 12 (4), 532–542.
62. Kaneko, T., Nakamura, Y., Sato, S., Minamisawa, K., Uchiumi, T., Sasamoto, S., Watanabe, A., Idesawa, K., Iriguchi, M., Kawashima, K., Kohara, M., Matsumoto, M., Shimpo, S., Tsuruoka, H., Wada, T., Yamada, M., and Tabata, S. (2002) Complete genomic sequence of nitrogen-fixing symbiotic bacterium *Bradyrhizobium japonicum* USDA 110. *DNA Res.* 9 (6), 189–197.
63. Kawarabayasi, Y., Sawada, M., Horikawa, H., Hino, Y., Yamamoto, S., Sekine, M., Baba, S., Kosugi, H., Hosoyama, A., Nagai, Y., Sakai, M., Ogura, K., Otsuka, R., Nakazawa, H., Takamiya, M., Ohfuku, Y., Funahashi, T., Tanaka, T., Kudoh, Y., Yamazaki, J., Kushida, N., Oguchi, A., Aoki, K., and Kikuchi, H. (2002) Complete sequence and gene organization of the genome of a hyper-thermophilic archaeobacterium, *Pyrococcus horikoshii* OT3. *DNA Res* 5 (2), 55–76.
64. Paulsen, I. T., Seshadri, R., Nelson, K. E., Eisen, J. A., Heidelberg, J. F., Read, T. D., Dodson, R. J., Umayam, L., Brinkac, L. M., Beanan, M. J., Daugherty, S. C., Deboy, R. T., Durkin, A. S., Kolonay, J. F., Madupu, R., Nelson, W. C., Ayodeji, B., Kraul, M., Shetty, J., Malek, J., Van Aken, S. E., Riedmuller, S., Tettelin, H., Gill, S. R., White, O., Salzberg, S. L., Hoover, D. L., Lindler, L. E., Halling, S. M., Boyle, S. M., and Fraser, C. M. (2002) The *Brucella suis* genome reveals fundamental similarities between animal and plant pathogens and symbionts. *Proc. Natl. Acad. Sci. U.S.A.* 99 (20), 13148–13153.
65. Cohen, G. N., Barbe, V., Flament, D., Galperin, M., Heilig, R., Lecompte, O., Poch, O., Prieur, D., Querellou, J., Ripp, R., Thierry, J. C., Van der Oost, J., Weissenbach, J., Zivanovic, Y., and Forterre, P. (2003) An integrated analysis of the genome of the hyperthermophilic archaeon *Pyrococcus abyssi*. *Mol. Microbiol.* 47 (6), 1495–1512.
66. Mccammon, J. A., Gelin, B. R., Karplus, M., and Wolynes, P. G. (1976) Hinge-bending mode in lysozyme. *Nature* 262 (5566), 325–326.
67. Mao, B., Pear, M. R., Mccammon, J. A., and Quirocho, F. A. (1982) Hinge-bending in L-arabinose-binding protein - the venus-flytrap model. *J. Biol. Chem.* 257 (3), 1131–1133.
68. Mao, B., and Mccammon, J. A. (1984) Structural study of hinge bending in L-arabinose-binding protein. *J. Biol. Chem.* 259 (8), 4964–4970.